Faraday Discussions

Cite this: *Faraday Discuss.*, 2018, **208**, 187

PAPER

Time-resolved operando studies of carbon supported Pd nanoparticles under hydrogenation reactions by X-ray diffraction and absorption

Aram L. Bugaev, *[ab] Oleg A. Usoltsev, [a] Andrea Lazzarini, [c] Kirill A. Lomachenko, [d] Alexander A. Guda, [a] Riccardo Pellegrini, [e] Michele Carosso, [b] Jenny G. Vitillo, [bf] Elena Groppo, [b] Jeroen A. van Bokhoven, [gh] Alexander V. Soldatov [a] and Carlo Lamberti *[ai]

Received 16th December 2017, Accepted 5th January 2018

DOI: 10.1039/c7fd00211d

The formation of palladium hydride and carbide phases in palladium-based catalysts is a critical process that changes the catalytic performance and selectivity of the catalysts in important industrial reactions, such as the selective hydrogenation of alkynes or alkadienes. We present a comprehensive study of a 5 wt% carbon supported Pd nanoparticle (NP) catalyst in various environments by using *in situ* and *operando* X-ray absorption spectroscopy and diffraction, to determine the structure and evolution of palladium hydride and carbide phases, and their distribution throughout the NPs. We demonstrate how the simultaneous analysis of extended X-ray absorption fine structure (EXAFS) spectra and X-ray powder diffraction (XRPD) patterns allows discrimination between the inner "core" and outer "shell" regions of the NP during hydride phase formation at different temperatures and under different hydrogen pressures, indicating that the amount of hydrogen in the shell region of the NP is lower than that in the core. For palladium carbide, advanced analysis of X-ray absorption near-edge structure

[a]*The Smart Materials Research Center, Southern Federal University, Sladkova 178/24, Rostov-on-Don, 344090, Russia. E-mail: arambugaev@gmail.com; carlo.lamberti@unito.it*

[b]*Department of Chemistry, NIS Interdepartmental Centre and INSTM Reference Centre, University of Turin, via Quarello 15A, 10135 Turin, Italy*

[c]*Centre for Materials Science and Nanotechnology, Department of Chemistry, University of Oslo, Sem Saelands vei 26, 0315 Oslo, Norway*

[d]*European Synchrotron Radiation Facility (ESRF), 71 avenue des Martyrs, CS 40220, 38043 Grenoble Cedex 9, France*

[e]*Chimet SpA-Catalyst Division, via di Pescaiola 74, 52041 Viciomaggio Arezzo, Italy*

[f]*Department of Chemistry, University of Minnesota, 207 Pleasant Street S.E., Minneapolis, Minnesota 55455-0431, USA*

[g]*Institute for Chemical and Bioengineering, ETH Zurich, Vladimir-Prelog-Weg 1, 8093 Zurich, Switzerland*

[h]*Laboratory for Catalysis and Sustainable Chemistry, Paul Scherrer Institute, 5232 Villigen, Switzerland*

[i]*Department of Physics and CrisDi Interdepartmental Centre, University of Turin, via Pietro Giuria 1, 10125 Turin, Italy*

(XANES) spectra allows the detection of Pd–C bonds with carbon-containing molecules adsorbed at the surface of the NPs. In addition, H/Pd and C/Pd stoichiometries of PdH_x and PdC_y phases were obtained by using theoretical modelling and fitting of XANES spectra. Finally, the collection of *operando* time-resolved XRPD patterns (with a time resolution of 5 s) allowed the detection, during the ethylene hydrogenation reaction, of periodic oscillations in the NPs core lattice parameter, which were in phase with the MS signal of ethane (product) and in antiphase with the MS signal of H_2 (reactant), highlighting an interesting direct structure–reactivity relationship. The presented studies show how a careful combination of X-ray absorption and diffraction can differentiate the structure of the core, shell and surface of the palladium NPs under working conditions and prove their relevant roles in catalysis.

1. Introduction

Palladium-based materials, in particular supported nanoparticles (NPs), have numerous industrial applications, such as catalysts for selective hydrogenation reactions. Palladium is the metal of choice for semi-hydrogenation of alkynes and alkadienes in mixtures of alkyne/alkene and alkadiene/alkene, respectively.[1–4] Palladium is prone to the formation of carbides and hydrides and therefore, under reaction conditions, exposure of the catalyst to a mixture of H_2 and hydrocarbons may lead to the formation of palladium hydride[5–13] or carbide[5,12,14,15] phases, which may dramatically affect the catalytic activity and selectivity.[4,14] For catalytic applications, it is important to understand the role of surface, subsurface and bulk hydrogen and carbon atoms[14] and the molecular-level picture of the catalytic hydrogenation over palladium NPs, which are both still under debate.[4,14–18]

The formation of both palladium hydride and carbide phases increases the lattice parameter of palladium, which can be effectively detected by using X-ray powder diffraction (XRPD).[12,19,20] This technique provides structural information about the crystalline phases, characterizing the bulk region of the NP. However, XRPD does not provide information about the NP surface,[13] nor about the structure of small (<1.5 nm) NPs, which are too small to produce well-defined Bragg peaks.[21] For this reason, extended X-ray absorption fine structure (EXAFS)[22–24] is widely applied for characterizing nanostructured samples.[25–29] This technique yields averaged interatomic distances and coordination numbers around a specific atom type, does not require long range order, and is applicable to both crystalline and amorphous materials. As XRPD and EXAFS techniques are based on the scattering of photons and backscattering of photoelectrons respectively, they are mostly sensitive to the heaviest atoms of the studied structure, being much less efficient (or almost inefficient) in detecting low Z atoms, such as carbon and hydrogen, present in metal carbides and hydrides, respectively. Unambiguous detection of hydride and carbide phases can be achieved by using X-ray absorption near-edge structure (XANES) spectroscopy, which covers a short 30–50 eV range above the absorption edge.[30–40] As we have demonstrated in previous works, XANES is able to distinguish Pd–H and Pd–C bonds *via* the difference in the structure of the unoccupied electronic states of palladium.[6,12,41]

Here, we report the formation of palladium hydrides and carbides in palladium NPs in alkene and alkyne hydrogenation reactions, using *in situ* and *operando* synchrotron-based XRPD and X-ray absorption spectroscopy (XAS). Through applying simultaneous XRPD and EXAFS, we observed the formation of a core–shell structure in the Pd NPs upon hydride phase formation. For carbide formation, additional XANES analysis to XRPD and EXAFS allowed the observation of the surface adsorbed carbon-containing molecules. In addition, we have developed a method which allowed us to estimate the H/Pd and C/Pd stoichiometries of PdH_x and PdC_y phases, through modelling and fitting the XANES spectra. Finally, the application of *operando* XRPD during the oscillatory reaction of ethylene to ethane conversion demonstrated that not only the surface, but also the core of the NPs undergoes rapid structural changes, which correlates with the catalytic activity of the sample, highlighting a direct structure–reactivity relationship.

2. Experimental and methods

2.1. Sample preparation

The Pd/C catalyst investigated in this study has been prepared and supplied by Chimet S.p.A: product D1190 from the Chimet catalyst library (http://www.chimet.com/). It is a 5 wt% Pd on carbon powder catalyst (hereinafter referred as Pd/C) prepared following the deposition–precipitation method[42] on a wood-origin activated carbon (specific surface area = 980 $m^2\ g^{-1}$; pore volume = 0.62 $cm^3\ g^{-1}$).[43,44] TEM characterization of the catalyst resulted in a narrow particle size distribution with size $\langle D \rangle = 2.6$ nm with the standard deviation of 0.4 nm, as pointed out in a previous work.[13] The palladium black sample has been prepared following a procedure similar to that adopted for the catalyst preparation, but omitting the support, and successively reduced in H_2 at 120 °C, resulting in a stable bulk Pd^0 phase.

2.2. *In situ* X-ray powder diffraction and X-ray absorption spectroscopy setup

Both XRPD and Pd *K*-edge XAS data were collected at the BM01B[45,46] beamline (SNBL, now moved to the BM31 port) of the ESRF synchrotron (Grenoble, France). The beamline allows fast (less than 1 minute) plug and play switches between XRPD and XAS setups, allowing the measurement for each reaction condition (temperature and gas composition) of both X-ray diffraction and absorption data.[12,13,47]

For *in situ* experiments, a boron glass capillary 1.0 mm in diameter filled with the catalyst powder, oriented horizontally and perpendicularly to the X-ray beam, was employed. A gas blower was positioned above the sample to define the temperature during the experiment. The capillary was glued into a metal holder connected to a pressurized setup, which allowed remote control of the gas mixture composition (H_2 and/or C_2H_2) and pressure inside the capillary. The basal pressure, which was reached by using a scroll pump, was lower than 0.1 mbar. The surface Pd-oxide layer formed on the palladium NPs upon air exposure,[48] was removed by performing a pretreatment at 125 °C in 200 mbar of pure H_2 for 30 minutes before data collection. For *operando* experiments, the 1.0 mm capillary was fed with the desired gas mixture (He, H_2 and/or C_2H_4) using

calibrated gas mass-flow controllers, while the composition of the gas outlet from the capillary was monitored by means of mass spectrometry (MS) measured by using a Pfeiffer Omnistar MS.

X-ray powder diffraction patterns were collected using $\lambda = 0.50544(2)$ Å radiation, selected by a Si(111) channel-cut monochromator. A CMOS-Dexela 2D detector was positioned at a distance of 250.24(7) mm from the sample, resulting in a 2θ range from 5° to 52°, corresponding to a 5.79 to 0.57 Å d-spacing interval. The values of λ, of the sample to detector distance, and of the detectors tilts have been optimized by Rietveld refinement of NIST LaB_6 and Si samples and kept fixed in the refinement of the Pd/C samples. For better statistics, 20 diffraction images and 20 dark images (with the X-ray shutter closed) with an acquisition time of 1 s were averaged in all cases. For the time-resolved *operando* experiment, we were collecting 100 subsequent patterns with 5 s time-resolution, followed by 100 dark patterns.

XAS spectra at the Pd *K*-edge were obtained in the transmission mode through continuous scanning of the double crystal Si(111) monochromator from 24 100 to 25 400 eV taking 5 minutes per spectrum. Pd foil was measured simultaneously with each spectrum for energy calibration using a third ionization chamber.[49] Detuning monochromator crystals of 20% from the maximum intensity makes the contribution of the third harmonic at 75 000 eV negligible.

2.3. Volumetric measurements

Hydrogen sorption isotherms were measured using Micromeritics ASAP2020 volumetric apparatus. The instrument was equipped with 4 pressure transducers, allowing the investigation of the sorption process at very low equilibrium pressures (down to 10^{-4} mbar). Prior to the measurements, the Pd/C powders (1.4 g) were activated on a vacuum line equipped with a turbomolecular pump ($P < 10^{-4}$ mbar): after degassing at 120 °C for 3 h, the sample was subjected to two H_2 absorption/desorption cycles at 120 °C in hydrogen (absorption pressure: ~100 mbar, desorption pressure: dynamic vacuum) to ensure full reduction of the palladium NPs. Then the sample was exposed to 100 mbar of H_2 and cooled down to room temperature. The sample was successively transferred in the measurement cell inside a glove box (M Braun Lab Star Glove Box supplied with pure 5.5 grade N_2, <0.5 ppm O_2, <0.5 ppm H_2O) and then degassed at room temperature for 1 h on the volumetric apparatus. The H_2 uptake of the bare carbon support was measured under the same conditions adopted for the Pd/C catalyst, after activation under dynamic vacuum at 120 °C overnight. The isotherms reported in the following for the Pd/C systems were obtained from the measured ones after subtraction of the H_2 uptake measured under the same conditions for the activated carbon support.

2.4. EXAFS, XANES and XRPD data analysis

X-ray absorption spectra were analyzed in the Demeter 0.9.21 package[50] including background subtraction, normalization, energy calibration, and single-shell Fourier analysis. A real space data fitting in the *R*-range from 1.5 to 3.2 Å was performed on the Fourier-transformed k^2-weighted, phase uncorrected, data in the k-range from 5.0 to 12.0 $Å^{-1}$, with the width of the window slope $dk = 1$ $Å^{-1}$, corresponding to the number of independent points $2\Delta k\Delta R/\pi > 7$. The low k-

region (2–5 $Å^{-1}$) was intentionally excluded from the analysis to minimize the Pd–C contribution from interaction of the NPs with the support. The fit included four parameters: the first shell Pd–Pd interatomic distance (R_{Pd-Pd}), the Debye–Waller factor (σ^2), the energy shift (ΔE_0) and the coordination number (N). The parameters ΔE_0 and N were considered as common variables for all spectra. The value of the passive electron amplitude reduction factor[51] ${S_0}^2 = 0.83 \pm 0.03$ was obtained by fitting the spectrum of Pd-foil and kept constant in the optimization of all the spectra collected on the Pd-catalyst. Experimental spectra were fitted in R-space using theoretical amplitudes and phases calculated by using the FEFF6 code.[52]

VASP 5.3 code[53–55] with a PBE exchange–correlation potential,[56] was used to optimize the geometries of the PdH_x and PdC_y phases. DFT-optimized PdH_x and PdC_y structures were then used for XANES calculation by using the FDMNES code.[36–40] Each spectrum, except the pure metallic one, was calculated by averaging 32 separate theoretical spectra for each Pd atom in the optimized supercell. Calculations were performed within the finite difference approach in full potential. A 6 Å cluster around the Pd absorbing atom was used in all simulations.

The fitting of experimental spectra by theoretical ones was performed by using a multidimensional interpolation method implemented in the FitIt-3 code.[57,58] Initially calculated spectra for given concentrations x, y in PdH_x, PdC_y ($x = 0$, 0.125, 0.250, 0.500; $y = 0$, 0.063, 0.125, 0.250) were used as interpolation nodes to obtain spectra for all intermediate concentrations. To exclude systematic errors and increase precision, fitting was performed for difference XANES spectra. To plot the experimental difference spectra, we subtracted the spectrum of initial metallic palladium NPs measured in vacuum from all other spectra, while the theoretical ones were obtained after subtracting the fitted theoretical spectrum of metallic palladium NPs.

2D XRPD patterns were processed by using PyFAI[59] software which executes fast averaging, background subtraction and integration of images to obtain $I(2\theta)$ patterns. Rietveld refinement of static XRPD patterns was performed with Jana2006 code.[60] Profile parameters were optimized by fitting the diffraction patterns of the metallic and of the most hydrogenated samples at each temperature. In the final refinement, we optimized the fractions of α- and β-phases and the cell parameters corresponding to each phase. The time-resolved data were analysed by a linear combination fitting.

3. Results and discussion

3.1. Core–shell structures during hydride formation in palladium nanoparticles

Palladium hydrides (PdH_x) may exist as two phases, named α and β, depending on the stoichiometric atomic ratio x.[61] For bulk palladium, the α-phase is present for values $0 < x \leq 0.03$, while the β-phase forms for values $x \geq 0.58$. Both phases are present for the intermediate values, which is often referred to as the *plateau* in the hydrogen isotherm diagram. From a crystallographic point of view, PdH_x exhibits the same fcc space group as Pd metal with an increased lattice parameter (a), that shows a stepwise behaviour at x values corresponding to the formation of α- and β-phases, while within each of the phases it linearly increases with x. The thermodynamics of hydrogen absorption of Pd NPs differ from that of palladium bulk due to the considerable contribution of the surface.[9,13,62] The typical phase

separation was observed in Pd NPs down to nanometer size,[21,63] but the relationship between hydrogen equilibrium pressure (EP) and H loading (x) differs significantly from the bulk and strongly depends on the size and shape of the NPs.[7,64,65] This affects both the maximum x value in the β-phase, and the extension of the x-interval of coexistence of the two α- and β-phases in the plateau.

XRPD (Fig. 1a) monitors the increase of the cell parameter a during the hydride formation, and is able to discriminate α and β phases, but it is scarcely informative for NPs smaller than 1 nm[21,63] (that do not contribute to the Bragg reflections) and to the external shell of NPs (because of disorder effects intrinsic of surface layers).[13] Being element specific,[22–29] EXAFS (Fig. 1b and c) probes the local environment around the Pd absorbing atom, yielding average R_{Pd-Pd} values, coordination numbers and Debye–Waller parameters, and providing important complementary information on the surface of the NPs,[13,66–75] which is merged with the information on the core. Complementary volumetric measurements provide quantitative information on the x stoichiometry at given temperature and H_2-EP values, provided that the hydrogen uptake from the carbon support is properly taken into account.[13,76,77]

Fig. 2 reports the XRPD (a), Pd K-edge XANES (b) and EXAFS (c) isotherms, collected at 22 °C on Pd/C of the PdH_x formation obtained by progressively increasing the H_2-EP from 0 to 1000 mbar. These, almost simultaneous, X-ray absorption/diffraction experiments have been repeated for the isotherms at 1, 22, 53, 62 and 85 °C (Fig. 2a and b) and duplicated with independent laboratory volumetric measurements (see Fig. 2c).

Fig. 2a and b report the dependence of the cell parameter, a, and the R_{Pd-Pd} value in the different points of the α/β phase diagrams of the PdH_x system as obtained from Rietveld refinement of XRPD and the first-shell analysis of the whole set of EXAFS data, respectively, collected at different H_2-EP during the five isotherms. At all investigated temperatures, the lattice expansion observed during the PdH_x phase formation is accompanied by an increase in the Debye–Waller parameter.[13] Being a phase-specific technique, XRPD is able to analyze separately the α- and β-hydride phases present in the sample at each point of the isotherm. The relative concentrations of the α- and β-phases and the cell parameters within each phase have been determined by a 2-phases Rietveld refinement procedure.[13] The structural isotherms obtained from XRPD have been plotted in Fig. 2a in a way that is directly comparable with those obtained from the EXAFS analysis (Fig. 2b) by reporting the averaged cell parameter as a weighted sum

$$a = (1 - n)a_\alpha + na_\beta, \quad (1)$$

where a_α and a_β are the refined lattice parameters of the α- and β-phases, respectively, and n the refined fraction of the β-phase.

The Pd-specific pressure–composition isotherms for the Pd NPs, reported in Fig. 2c, have been obtained by: (i) subtracting from the raw isotherms collected on the Pd/C samples the analogous isotherms collected on the bare carbon support and (ii) correcting for the amount of hydrogen uptake at low pressure, which corresponds to the formation of a hydrogen layer on the surface of the NPs, and not to the formation of the Pd-hydride phase.[13] The nanometric dimensions of the Pd NPs resulted in a maximum uptake in the β-phase of $PdH_{0.4}$ lower than $PdH_{0.6}$ reported for bulk palladium.[78–80] This observation reflects the lower number of

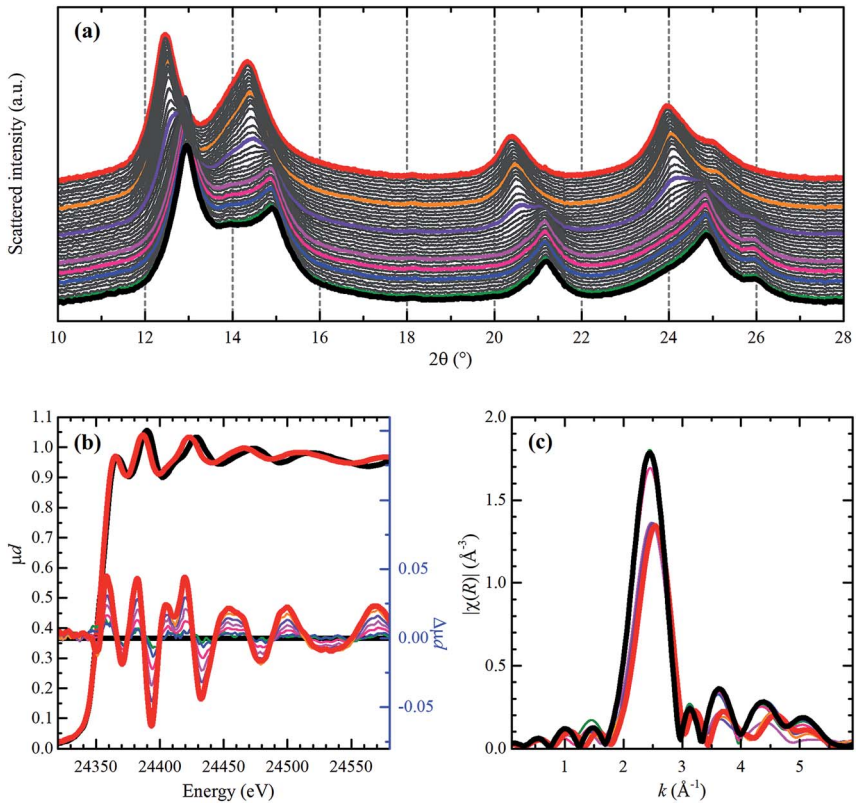

Fig. 1 Evolution of the diffraction data and of the Pd *K*-edge X-ray absorption spectra along the Pd-hydride formation in Pd NPs at 22 °C obtained by increasing the H_2-EP in the pressure range from 0 (bold black) to 1000 (bold red) mbar. Part (a) the whole series of the XRPD patterns where coloured intermediate patterns correspond to 1 (green), 10 (blue), 17 (pink), 20 (magenta), 25 (violet) and 100 (orange) mbar. Part (b) XANES spectra (left ordinate axis) obtained at H_2-EP of 0 (black curve) and 1000 mbar (red curve) and ΔXANES spectra (right ordinate axis) obtained by subtracting the spectrum of the metal phase. Part (c) Fourier-transformed k^2-weighted, phase uncorrected, $\chi(k)$ EXAFS functions recorded under the same conditions. For the sake of clarity only a fraction of the measured spectra is reported in parts (b–c), with the same colour code as for the diffraction patterns reported in part (a). Previously unpublished figure reporting data published in ref. 13.

interstitial sites per mass of palladium (related to the higher surface to volume ratio)[80] and the lower critical temperature[64,81,82] of Pd NPs with respect to the bulk.

The pressure–structure isotherms shown in Fig. 2a and b are similar to the pressure–composition curves obtained from volumetric measurements (Fig. 2c), which gives information about the H/Pd ratio at any given temperature and pressure. All of the isotherms are characterized by three distinct regions: (i) the pre-plateau region, related to the formation of the α-phase (yellow region); (ii) the plateau, corresponding to the gradual phase transition from the solid solution to the β-phase (white region); (iii) the post-plateau region, where the solid solution of hydrogen in the metal hydride is formed (red region).[80] As it is widely reported for bulk palladium, the pressure corresponding to the plateau increases with the temperature and at the same time the miscibility gap of the solid solution with the

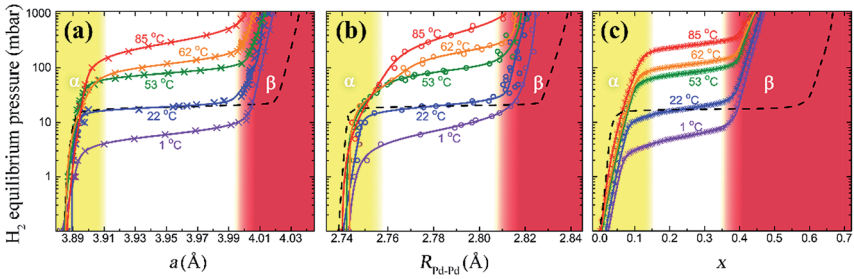

Fig. 2 α/β phase diagrams of the PdH_x system evidenced in the pressure–*a*, pressure–R_{Pd-Pd}, and pressure–*x* isotherms obtained from XRPD (a), EXAFS (b), and Pd-specific H_2-adsorption volumetry (c) for Pd/C at different temperatures (colored scatters) and palladium bulk (Pd-black) (black dashed line) at 22 °C. Only the absorption branches are reported for each temperature. Solid colored lines correspond to the best fits by a model double-exponential function. The abscissa of part (a) is the averaged cell parameter defined in eqn (1). The yellow, white and red regions define qualitatively pure α-, mixed-, and pure β-phases, respectively, for the Pd/C sample. Adapted with permission from ref. 13, copyright ACS 2017.

hydride phase decreases.[61] As a consequence of the nanometric size, for Pd NPs the hydrogen-uptake and the average lattice parameters at the end of each plateau are lower than those for bulk palladium at the same temperature.[13,79,80,83] This effect is evident when comparing the structural and compositional isotherms obtained at 22 °C for Pd/C (blue scatters in Fig. 2) and palladium black (dashed black line in Fig. 2). However, for Pd/C, the first shell EXAFS data themselves (Fig. 2b) exhibit a less defined plateau than the corresponding XRPD data (Fig. 2a). The plateau of the isotherms obtained by EXAFS, for Pd/C, are spanned in a wider pressure range with respect to the same plateau observed by XRPD at all the investigated temperatures. This discrepancy is absent for palladium black, indicating that it is a characteristic feature of the sample, and not a result of a different method.

The systematic difference in the behavior of the first shell EXAFS and XRPD data can be quantified by plotting the R_{Pd-Pd} value extracted from the XRPD isotherm ($R_{Pd-Pd} = a/\sqrt{2}$) together with the EXAFS isotherm, see Fig. 3, green and black curves, respectively. This difference can be explained by considering that the PdH_x NPs have a core–shell structure, with a crystalline core that contributes both to the Bragg reflections in the XRPD patterns and to the first shell Pd–Pd distance obtained by using EXAFS, and an amorphous shell that contributes only to the latter observable.[13] This model is in line with the evidence that, for Pd NPs with an average size of 1 nm[9] (which do not give well-defined Bragg peaks),[21,63] the α–β phase separation does not exist and the pressure–composition isotherms lack the plateau region. The theoretical Pd–Pd distance in the amorphous shell (R_{Pd-Pd}^{shell}) has been derived from the combined XRPD and EXAFS data, according to the following expression:[13]

$$CR_{Pd-Pd}^{shell} = R_{Pd-Pd}^{EXAFS} - (1 - C)\frac{1}{\sqrt{2}}a, \quad (2)$$

where *C* is the fraction of atoms located in the amorphous shell. The red, blue and orange curves in Fig. 3 report the R_{Pd-Pd}^{shell} values obtained for the 22 °C isotherm

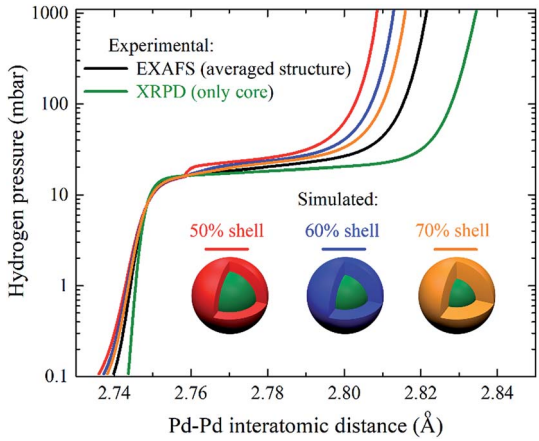

Fig. 3 Simulated pressure–structure isotherms at 22 °C of hydride formation in the shell of the palladium particles assuming core/shell ratios of 50/50 (red), 40/60 (blue) and 30/70 (orange) derived from XRPD-(green) and EXAFS-(black) based experimental isotherms.

assuming a C fraction of 0.5, 0.6 and 0.7, respectively. The shell absorbs hydrogen gradually, and the corresponding simulated isotherms result in a much less-defined α–β-phase transition.

Summarizing, the synergic coupling of the three techniques highlights clear differences in the structural and electronic configuration of the palladium atoms in the shell and in the core of the NPs during the Pd–PdH$_x$ phase transition.[13] The data reported in Fig. 3 represent an important estimation of the R_{Pd-Pd} distance at the surface of the NP, *i.e.* the R_{Pd-Pd} of the actual active phase, where hydrogenation reactions occur.

3.2. Carbide formation in the core, in the shell and at the surface of Pd NPs

As shown in the previous section, both XRPD and EXAFS indicate the formation of hydride phases by monitoring the increase of the interatomic distances that occurs due to the insertion of the hydrogen atoms into the palladium lattice. However, under hydrogenation reaction conditions, a palladium catalyst is exposed to a mixture of several gasses, H_2/hydrocarbons.[2,3] Under these conditions, the formation of both palladium hydride and carbide phases is possible, which cannot be distinguished by standard EXAFS and XRPD analysis, as the lattice parameters for these phases are very similar, while amplitudes of photoelectron backscattering and photon scattering are much lower for H and C atoms than for Pd ones, not allowing their direct observation. However, direct observation of Pd–H and Pd–C bonds would be possible by analyzing XANES spectra, which are sensitive to the presence of unoccupied states that result from the mixing of Pd- and H- or C-orbitals.[12,41]

Fig. 4a shows the typical Pd K-edge XANES spectra of palladium NPs observed under vacuum conditions and after exposure of the sample to hydrogen and acetylene, to form hydride and carbide phases, respectively. The spectrum of PdH$_x$ shows a sharpening of the first XANES peak and shifting to lower energies by about 1 eV, the opposite behavior is observed in the spectra after exposing the

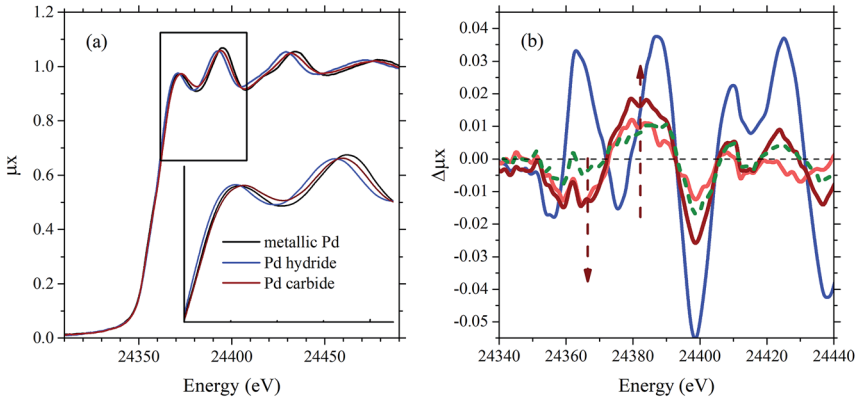

Fig. 4 Part (a): experimental spectra of palladium NPs under vacuum (black), under hydrogen (blue), and after 1 hour of total exposure to acetylene (dark-red). Part (b) shows the corresponding difference XANES spectra with addition of the spectrum after 15 minutes exposure to acetylene (light-red) and after subsequent treatment in H_2 and successive outgassing (green). All of the reported experiments have been performed with a sample temperature of 100 °C. See the orange triangles in Fig. 5 for the quantitative results of the ΔXANES modelling and fitting procedure.

sample to acetylene and carbide formation. For better appreciation and further quantitative analysis, we have considered the difference XANES spectra, shown in Fig. 4b, where the spectrum of Pd NPs under vacuum was subtracted from each of the other spectra. The typical features assigned to Pd–C bonds in the difference spectra are evolving with time, as shown by light red (15 minutes exposure to acetylene) and dark red (more than one hour exposure to acetylene) curves in Fig. 4b. In addition, partially inversed behavior is observed when the catalyst is subsequently treated with H_2 and evacuated (Fig. 4b, green curve).

The time evolution of Pd NPs upon exposure to hydrogen, acetylene and vacuum conditions was studied by applying three independent approaches and is summarized in Fig. 5. First, Rietveld refinement of XRPD patterns was performed to obtain the average cell parameter in the NPs, see grey circles in Fig. 5, obtained by applying eqn (1). Second, the first-shell Fourier analysis of EXAFS spectra provided the averaged Pd–Pd interatomic distances (Fig. 5, black squares). Finally, all experimental ΔXANES spectra were fitted (*vide infra*) by using the theoretically calculated ones to obtain the concentration of carbon atoms per palladium atom, C/Pd, *i.e.* the y stoichiometry of the PdC_y phase (Fig. 5, orange triangles).

In the 2 : 1 mixture of H_2 and C_2H_2 (green part in Fig. 5), the averaged lattice parameter in the NPs is increased by ~3%, with respect to pure palladium NPs, which is close to the values obtained in Section 3.1 for palladium hydride at 1000 mbar. In agreement with previous results,[12] the shape of the ΔXANES spectra (Fig. 4b, blue line) confirms that the hydride phase is formed under these conditions. In addition, a trial to fit the ΔXANES spectra by using the theoretical signal for palladium carbide resulted in unphysical negative y values (Fig. 5). The observed difference between the lattice expansion observed by using EXAFS and XRPD correlates with the core–shell structure of the PdH_x NPs (see Fig. 3).

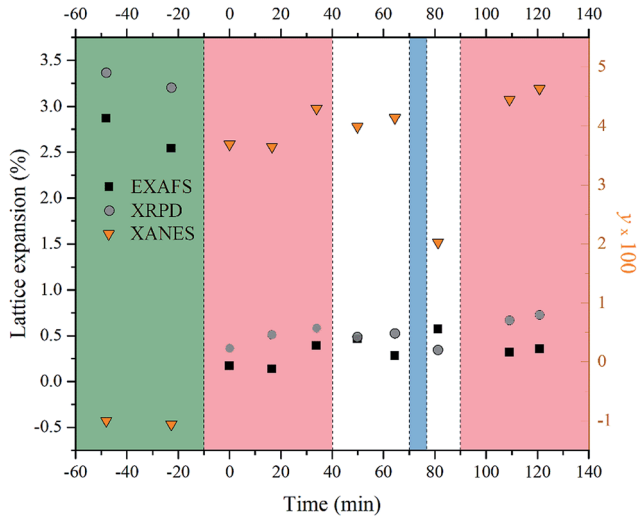

Fig. 5 Evolution of structural parameters obtained from XRPD, EXAFS and ΔXANES analysis. Left ordinate axis: variation of the R_{Pd-Pd} distance (black squares) obtained from the first-shell EXAFS-analysis and of the average lattice parameter obtained from XRPD refinement (gray circles). Right ordinate axis: stoichiometry of the PdC_y (in %) phase, determined by using ΔXANES modelling and fitting (orange triangles). Exposure of the sample to pure H_2, C_2H_2 and vacuum are highlighted by light-blue, light-red and white areas respectively. In the region below $t = 0$, the sample was exposed to 1 bar of a hydrogen/acetylene mixture in a 2 : 1 stoichiometric ratio (green area). All the reported experiments have been performed with a sample temperature of 100 °C.

The removal of H_2 from the feed mixture (first light-red part in Fig. 5), leads to a complete decomposition of the hydride phase, as all hydride features disappear from both the XANES and ΔXANES spectra. However, the interatomic distances are higher by 0.5% than in pure Pd NPs. This increase is explained by the formation of the second phase with an increased lattice parameter observed in the XRPD patterns. According to the shape of the ΔXANES curves this phase was assigned to palladium carbide. There is a slow increase of the lattice parameter of the carbidized sample with progressive C_2H_2 exposure time at 100 °C (light-red parts in Fig. 5) and that it is not reversed either by successive vacuum or treatment in H_2, see Fig. 5 white and light-blue parts, respectively.

To determine the evolution of the y stoichiometry in the PdC_y carbide phase, all experimental ΔXANES spectra were fitted by the theoretical ones applying a multidimensional interpolation approach. A set of model structures with different y values and lattice parameters (thus different $R_{Pd-Pd} = a/\sqrt{2}$) were initially optimized with the help of the VASP 5.3 code[53–55] and used for XANES calculation with the FDMNES code,[36–40] as described in Section 2.4. The calculated spectra were then taken as interpolation nodes in the two-dimensional (R_{Pd-Pd}, y) space, and used for the construction of a polynomial which describes the shape of the ΔXANES spectra for any of the R_{Pd-Pd} and y values. At the first step, we fitted the experimental XANES spectrum of Pd NPs under vacuum, and used the best fit theoretical spectrum to construct theoretical ΔXANES curves. All other spectra were fitted by minimizing the root-mean-square deviation $F(R_{Pd-Pd}, y)$ between the

theoretical and experimental ΔXANES spectra, varying R_{Pd-Pd} and y values defined as:

$$F(R_{Pd-Pd},\ y) = \frac{1}{\text{norm}}\sqrt{\sum_{i=1}^{N}[\Delta\text{XANES}^{exp}(E_i) - \Delta\text{XANES}^{theo}(E_i, R_{Pd-Pd},\ y)]^2} \quad (3)$$

where E_i are the energy values where the experimental curves have been sampled, $E_1 = 24\ 340$ eV and $E_N = 24\ 440$ eV are the first and the last experimental points considered in the fit and N is the total number of experimental points. The 2D distributions of $F(R_{Pd-Pd}, y)$ for selected spectra are shown in Fig. 6. For the spectrum taken in H_2 ($t = -22$ min), the minimum of F is achieved for the increased R_{Pd-Pd} and indicates zero carbon incorporation ($y = -0.01$, *i.e.* $y = 0$ within the experimental incertitude). This result represents a consistence test of the adopted method, as no Pd-carbide phase is expected to be formed in these conditions.[12] An increase of the carbon incorporation is observed after acetylene exposure and the position of the minimum of F shifts towards higher y values from the spectrum taken at $t = 0$, to that taken at $t = 120$ min, where the time corresponds to the starting time of each spectrum. The only deviation from the increasing y trend is observed after H_2 treatment of the sample ($t = 81$ min), which leads to a decrease of y by a factor of 2. This difference is observed only in the XANES spectra, while the EXAFS and XRPD values are not affected by H_2

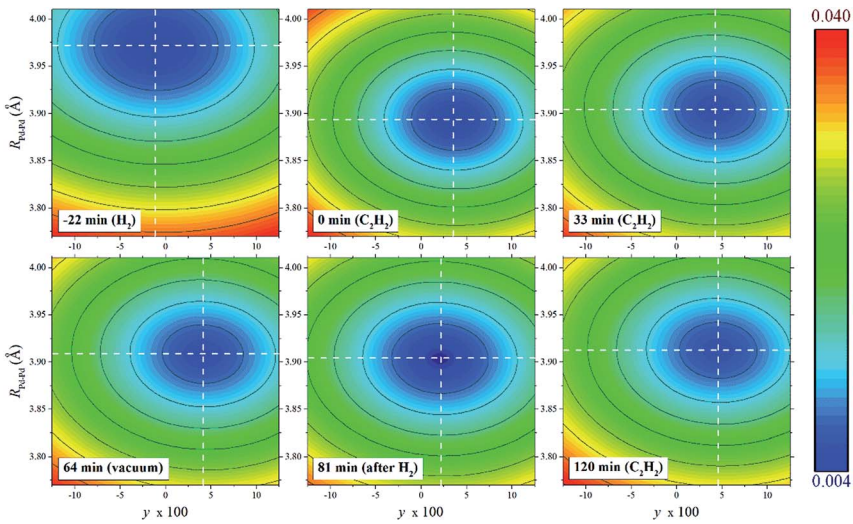

Fig. 6 2D plots of the $F(R_{Pd-Pd}, y)$ root-mean-square deviation function between theoretical and experimental ΔXANES spectra, defined in eqn (3) for different experimental curves collected at a time indicated in the bottom left corner and referred to the feeding conditions defined in Fig. 5. The white dotted lines highlight the position of the minimum for each spectrum corresponding to the best estimation for R_{Pd-Pd} and y values of the PdC_y phase in the corresponding experimental conditions. The used color scale is quantified in the right panel. The fact that there is one order of magnitude in the intensity differences between the blue and red regions implies that in all cases we are dealing with quite stable minima.

treatment. The reason for such behavior is that the XANES spectra are sensitive not only to carbon atoms, which are inserted in the interstitials of the palladium lattice forming a palladium carbide phase, but also the surface adsorbed acetylene molecules, which do not affect the interatomic distance while they contribute to the number of Pd–C bonds. H_2 treatment can be therefore used to remove the surface acetylene through its hydrogenation to ethylene and ethane, while it does not remove the carbon atoms from the palladium lattice.[15] This unambiguously shows that the use of XANES spectra, in addition to EXAFS and XRPD, allows the extraction of information on the structure of surface atoms, in addition to the core–shell structure, which is revealed by the combination of the latter two,[13] see Section 3.1.

In this case XANES was used as a completely independent technique that provides both structure (R_{Pd-Pd}), and stoichiometry (y) of the PdC_y phase. However, given that Fourier-analysis of the EXAFS data has been performed, the R_{Pd-Pd} values can be fixed to those obtained by EXAFS analysis. For the current data set, as can be seen from Fig. 6, $F(R_{Pd-Pd}, y)$ functions are symmetric with respect to horizontal and vertical dashed lines passing through the minimal point of each spectrum. Thus, for this particular case, having an error in the determination of the R_{Pd-Pd} value does not affect the position of the minimum along the y axis, while in the case of an asymmetric distribution of the F function, the use of EXAFS interatomic distances would have been more important.

3.3. *Operando* XRPD study during the hydrogenation of ethylene: evidence for structural and catalytic oscillating behavior

Operando XRPD patterns were collected every 5 s under steady state gas feeding to the Pd/C catalyst (6, 39 and 5 ml min^{-1} for He, H_2 and C_2H_4, respectively) allowing monitoring of the structural parameters of the core of the Pd NP during ethylene hydrogenation at 80 °C, see Fig. 7. Part (a) reports the 2θ region covering the (220), (311) and (222) Bragg reflections of palladium for a series of 10 subsequent diffraction patterns (from $t = 100$ to $t = 150$ s). These data indicate that, during steady state feeding conditions, the core structure of the Pd NPs is not stable, but changes with time. Fig. 7b, left ordinate axis, reports the time evolution of the average lattice parameter, obtained using eqn (1). The structural changes are not random, but follow a clear oscillating behavior with a period of about 150 s. The periodic lattice parameter variation is due to the periodic change in the relative fraction of the β- and α-phases of palladium hydride (see Section 3.1 in general and Fig. 2a in particular) and here reported in Fig. 7b, right ordinate axis. The most interesting aspect of this experiment is the fact that the same periodic oscillations of non-regular shape were observed by using MS monitoring for both the reactants and products, see Fig. 7c. Indeed, the MS signal of the C_2H_6 product ($m/Z = 30$) is in perfect phase with the oscillation of the fraction of the β-phase of palladium hydride obtained by using XRPD, while the MS signal of the H_2 reactant ($m/Z = 2$) is in perfect antiphase. Although Fig. 7b and c report only 10 min, the oscillations were stable for 30 minutes, until we changed the feed.

This evidence is a direct undisputed proof of a strong structure–reactivity relationship between the structure of the core of the PdH_x NPs and the catalyst activity in the ethylene hydrogenation reaction. Also evident is the fact that the catalyst is more active in the $H_2 + C_2H_4 \rightarrow C_2H_6$ reaction when the core of the

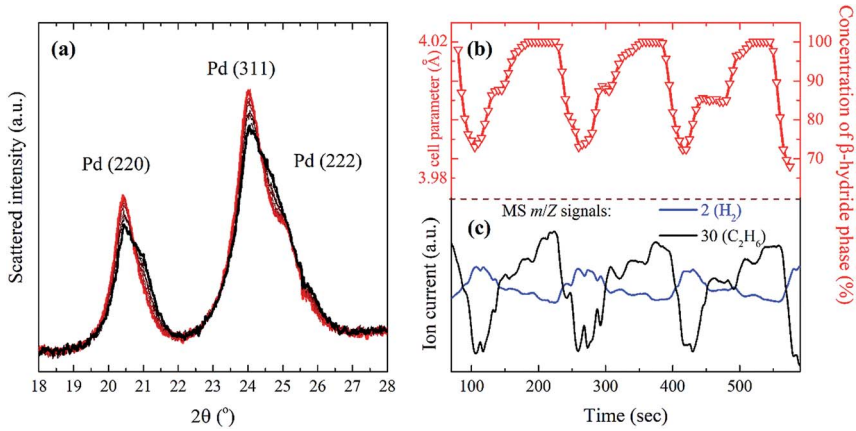

Fig. 7 Time resolved, *operando* XRPD study during the ethylene hydrogenation reaction at 80 °C on a Pd/C catalyst performed under steady state feeding conditions: (6, 39 and 5 ml min^{-1} for He, H_2 and C_2H_4, respectively). Part (a): selection of XRPD patterns at significant times (from $t = 100$ s, black curve, to $t = 150$ s, red curve), evidencing structural changes along the reaction monitored in the 2θ range of the most significant Pd Bragg reflections. Part (b): time evolution of the averaged Pd lattice parameter, see eqn (1), and of the fraction of the β-phase of PdH_x left and right ordinate axis, respectively. Part (c): time evolution of the catalyst activity monitored by using MS showing a reactant (H_2, $m/Z = 2$) and a product (C_2H_6, $m/Z = 30$).

PdH_x NPs is in the β-phase, in agreement with previous findings.[14] However, the interpretation of the observed oscillating behavior from an atomistic point of view is not straightforward.The set of experimental data summarized in Fig. 7 can be rationalized by the considerations discussed in the following.

In the case of NPs fully in the β-phase (*e.g.* at $t = 200$ s in Fig. 7b and c), catalyst activity is maximal. Owing to the exothermicity of the ethylene hydrogenation reaction ($\Delta H^0 = -136$ kJ mol^{-1}),[84,85] the NPs undergo a local temperature increase, which results in a partial hydrogen desorption (see Fig. 2), that in turn results in a decrease of the fraction of the β-phase, down to 70% (at $t = 270$ s). The lower availability of atomic hydrogen in the NP core slows down the reaction, which drives a local temperature decrease, further slowing the reaction and increasing the average H_2 partial pressure in the feed. These facts reform the β-phase restoring the higher catalytic activity ($t = 355$ s). The fact that heating of the NPs plays a role is indicated in that after completing the β-phase formation, there is a continued increase in activity, indicated by the growing ethane signal.

4. Conclusions

In the present study, we have combined synchrotron-based *in situ* and *operando*, almost simultaneous, X-ray diffraction and absorption data collection to laboratory volumetric measurements to shed light on the structure and the stoichiometry of PdH_x and PdC_y phases of Pd NPs during hydrocarbon hydrogenation reactions on a Pd/C catalyst. Six main results have been achieved.

First, the systematic *in situ* XRPD, EXAFS and volumetric analysis in a wide range of sample temperatures and H_2 equilibrium pressures, allowed us to follow

the α–β phase transition diagram of Pd NPs. The structural/stoichiometric α–β phase diagram reported in Fig. 2a–c allowed us to determine the PdH_x stoichiometry from an EXAFS or an XRPD structural datum. Second, the almost simultaneous EXAFS and XRPD set of data allowed us to discriminate the ordered NP core from the disordered shell and to reconstruct the R_{Pd-Pd} distance at the amorphous surface of the NP, *i.e.* the R_{Pd-Pd} of the actual active phase, where hydrogenation reactions occur (Fig. 3). Third, while both XRPD and EXAFS are unable to discriminate between palladium hydride and carbide phases, XANES provides unambiguous detection of hydride and carbide phases (Fig. 4a), with the discrimination ability being more evident when the data are reported in difference mode (ΔXANES, Fig. 4b). Fourth, the combined use of XRPD, EXAFS and XANES, supported by corresponding simulations,[86] allowed us to obtain both the core and shell structures and the average y stoichiometry of the PdC_y phase formed upon exposure of Pd NPs to C_2H_2 for increasing times (Fig. 5 and 6). Fifth, advanced analysis of the ΔXANES spectra allows the detection of carbon-containing molecules adsorbed at the surface of the NPs. Finally, the collection of *operando* XRPD patterns allowed us to observe, during the ethylene hydrogenation reaction, periodic oscillations of a non-regular shape of the NPs core lattice parameter, that resulted to be in phase with the MS signal of the C_2H_6 product and in antiphase with the MS signal of the H_2 reactant (Fig. 7), highlighting an interesting direct structure–reactivity relationship.

A repetition rate of 0.2 Hz (one XRPD pattern every 5 s) was needed to follow the structural oscillation of the core. Palladium hydride phase changes are observed in parallel with the ethylene hydrogenation activity. Local temperature and hydrogen concentrations drive the formation and disappearance of the β-phase and catalytic activity.

Acknowledgements

A. L. B., O. A. U., A. A. G., A. V. S., and C. L. acknowledge the Russian Ministry of Education and Science for financial support (Project RFMEFI58417X0029, Agreement 14.584.21.0029). We are indebted to Vladimir Dmitriev, Herman Emerich, Wouter van Beek and Michela Brunelli for their friendly and competent support during the experiments performed at the BM01B (now BM31) beamline of the ESRF.

Notes and references

1 A. Molnar, A. Sarkany and M. Varga, *J. Mol. Catal. A: Chem.*, 2001, **173**, 185–221.
2 A. Borodzinki, *Catal. Rev.: Sci. Eng.*, 2006, **48**, 91–144.
3 A. Borodzinski and G. C. Bond, *Catal. Rev.: Sci. Eng.*, 2008, **50**, 379–469.
4 M. Armbruster, M. Behrens, F. Cinquini, K. Fottinger, Y. Grin, A. Haghofer, B. Klotzer, A. Knop-Gericke, H. Lorenz, A. Ota, S. Penner, J. Prinz, C. Rameshan, Z. Revay, D. Rosenthal, N. Rupprechter, P. Sautet, R. Schlogl, L. D. Shao, L. Szentmiklosi, D. Teschner, D. Torres, R. Wagner, R. Widmer and G. Wowsnick, *ChemCatChem*, 2012, **4**, 1048–1063.
5 J. A. McCaulley, *J. Phys. Chem.*, 1993, **97**, 10372–10379.
6 A. V. Soldatov, S. Dellalonga and A. Bianconi, *Solid State Commun.*, 1993, **85**, 863–868.

7 S. Kishore, J. A. Nelson, J. H. Adair and P. C. Eklund, *J. Alloys Compd.*, 2005, **389**, 234–242.
8 M. Yamauchi, R. Ikeda, H. Kitagawa and M. Takata, *J. Phys. Chem. C*, 2008, **112**, 3294–3299.
9 C. Langhammer, E. M. Larsson, B. Kasemo and I. Zoric, *Nano Lett.*, 2010, **10**, 3529–3538.
10 T. Shegai and C. Langhammer, *Adv. Mater.*, 2011, **23**, 4409–4414.
11 A. L. Bugaev, A. A. Guda, K. A. Lomachenko, V. V. Srabionyan, L. A. Bugaev, A. V. Soldatov, C. Lamberti, V. P. Dmitriev and J. A. van Bokhoven, *J. Phys. Chem. C*, 2014, **118**, 10416–10423.
12 A. L. Bugaev, A. A. Guda, A. Lazzarini, K. A. Lomachenko, E. Groppo, R. Pellegrini, A. Piovano, H. Emerich, A. V. Soldatov, L. A. Bugaev, V. P. Dmitriev, J. A. van Bokhoven and C. Lamberti, *Catal. Today*, 2017, **283**, 119–126.
13 A. L. Bugaev, A. A. Guda, K. A. Lomachenko, V. V. Shapovalov, A. Lazzarini, J. G. Vitillo, L. A. Bugaev, E. Groppo, R. Pellegrini, A. V. Soldatov, J. A. van Bokhoven and C. Lamberti, *J. Phys. Chem. C*, 2017, **121**, 18202–18213.
14 D. Teschner, J. Borsodi, A. Wootsch, Z. Revay, M. Havecker, A. Knop-Gericke, S. D. Jackson and R. Schlogl, *Science*, 2008, **320**, 86–89.
15 M. W. Tew, M. Nachtegaal, M. Janousch, T. Huthwelker and J. A. van Bokhoven, *Phys. Chem. Chem. Phys.*, 2012, **14**, 5761–5768.
16 D. Teschner, Z. Revay, J. Borsodi, M. Havecker, A. Knop-Gericke, R. Schlogl, D. Milroy, S. D. Jackson, D. Torres and P. Sautet, *Angew. Chem., Int. Ed.*, 2008, **47**, 9274–9278.
17 D. Teschner, J. Borsodi, Z. Kis, L. Szentmiklosi, Z. Revay, A. Knop-Gericke, R. Schlogl, D. Torres and P. Sautet, *J. Phys. Chem. C*, 2010, **114**, 2293–2299.
18 M. W. Tew, M. Janousch, T. Huthwelker and J. A. van Bokhoven, *J. Catal.*, 2011, **283**, 45–54.
19 W. Vogel, W. He, Q. H. Huang, Z. Q. Zou, X. G. Zhang and H. Yang, *Int. J. Hydrogen Energy*, 2010, **35**, 8609–8620.
20 Z. A. Chase, J. L. Fulton, D. M. Camaioni, D. H. Mei, M. Balasubramanian, V. T. Pham, C. Zhao, R. S. Weber, Y. Wang and J. A. Lercher, *J. Phys. Chem. C*, 2013, **117**, 17603–17612.
21 D. G. Narehood, S. Kishore, H. Goto, J. H. Adair, J. A. Nelson, H. R. Gutierrez and P. C. Eklund, *Int. J. Hydrogen Energy*, 2009, **34**, 952–960.
22 A. Filipponi, A. DiCicco and C. R. Natoli, *Phys. Rev. B: Condens. Matter Mater. Phys.*, 1995, **52**, 15122–15134.
23 J. J. Rehr and R. C. Albers, *Rev. Mod. Phys.*, 2000, **72**, 621–654.
24 J. A. van Bokhoven and C. Lamberti, *X-Ray Absorption and X-Ray Emission Spectroscopy: Theory and Applications*, John Wiley & Sons, Chichester, UK, 2016.
25 C. Lamberti, *Surf. Sci. Rep.*, 2004, **53**, 1–197.
26 S. Bordiga, E. Groppo, G. Agostini, J. A. van Bokhoven and C. Lamberti, *Chem. Rev.*, 2013, **113**, 1736–1850.
27 L. Mino, G. Agostini, E. Borfecchia, D. Gianolio, A. Piovano, E. Gallo and C. Lamberti, *J. Phys. D: Appl. Phys.*, 2013, **46**, 72.
28 C. Garino, E. Borfecchia, R. Gobetto, J. A. van Bokhoven and C. Lamberti, *Coord. Chem. Rev.*, 2014, **277**, 130–186.

29 C. Lamberti and J. A. van Bokhoven, in *X-Ray Absorption and X-Ray Emission Spectroscopy: Theory and Applications*, ed. J. A. van Bokhoven and C. Lamberti, John Wiley & Sons, Chichester, UK, 2016, vol. II, ch. 13, pp. 353–383.
30 A. Bianconi, J. Garcia and M. Benfatto, *Top. Curr. Chem.*, 1988, **145**, 29–67.
31 M. Benfatto and S. Della Longa, *J. Synchrotron Radiat.*, 2001, **8**, 1087–1094.
32 M. Benfatto, S. Della Longa and C. R. Natoli, *J. Synchrotron Radiat.*, 2003, **10**, 51–57.
33 C. R. Natoli, M. Benfatto, S. Della Longa and K. Hatada, *J. Synchrotron Radiat.*, 2003, **10**, 26–42.
34 A. L. Ankudinov, B. Ravel, J. J. Rehr and S. D. Conradson, *Phys. Rev. B: Condens. Matter Mater. Phys.*, 1998, **58**, 7565–7576.
35 J. J. Rehr and A. L. Ankudinov, *Coord. Chem. Rev.*, 2005, **249**, 131–140.
36 Y. Joly, *Phys. Rev. B: Condens. Matter Mater. Phys.*, 2001, **63**, 125120.
37 O. Bunau and Y. Joly, *J. Phys.: Condens. Matter*, 2009, **21**, 345501.
38 Y. Joly and S. Grenier, in *X-Ray Absorption and X-Ray Emission Spectroscopy: Theory and Applications*, ed. J. A. van Bokhoven and C. Lamberti, John Wiley & Sons, Chichester, UK, 2016, vol. I, ch. 4, pp. 73–97.
39 S. A. Guda, A. A. Guda, M. A. Soldatov, K. A. Lomachenko, A. L. Bugaev, C. Lamberti, W. Gawelda, C. Bressler, G. Smolentsev, A. V. Soldatov and Y. Joly, *J. Chem. Theory Comput.*, 2015, **11**, 4512–4521.
40 A. A. Guda, S. A. Guda, M. A. Soldatov, K. A. Lomachenko, A. L. Bugaev, C. Lamberti, W. Gawelda, C. Bressler, G. Smolentsev, A. V. Soldatov and Y. Joly, *J. Phys.: Conf. Ser.*, 2016, **712**, 012004.
41 A. L. Bugaev, V. V. Srabionyan, A. V. Soldatov, L. A. Bugaev and J. A. van Bokhoven, *J. Phys.: Conf. Ser.*, 2013, **430**, 012028.
42 G. Poncelet, P. Jacobs and P. Grange, *Preparation of catalysts III*, Elsevier, 1983.
43 G. Agostini, C. Lamberti, R. Pellegrini, G. Leofanti, F. Giannici, A. Longo and E. Groppo, *ACS Catal.*, 2014, **4**, 187–194.
44 A. Piovano, A. Lazzarini, R. Pellegrini, G. Leofanti, G. Agostini, S. Rudić, A. L. Bugaev, C. Lamberti and E. Groppo, *Adv. Condens. Matter Phys.*, 2015, **2015**, 803267.
45 W. van Beek, O. V. Safonova, G. Wiker and H. Emerich, *Phase Transitions*, 2011, **84**, 726–732.
46 P. M. Abdala, O. V. Safonova, G. Wiker, W. van Beek, H. Emerich, J. A. van Bokhoven, J. Sa, J. Szlachetko and M. Nachtegaal, *Chimia*, 2012, **66**, 699–705.
47 C. W. Andersen, E. Borfecchia, M. Bremholm, M. R. V. Jorgensen, P. N. R. Vennestrom, C. Lamberti, L. F. Lundegaard and B. B. Iversen, *Angew. Chem., Int. Ed.*, 2017, **56**, 10367–10372.
48 E. Groppo, G. Agostini, A. Piovano, N. B. Muddada, G. Leofanti, R. Pellegrini, G. Portale, A. Longo and C. Lamberti, *J. Catal.*, 2012, **287**, 44–54.
49 C. Lamberti, S. Bordiga, F. Bonino, C. Prestipino, G. Berlier, L. Capello, F. D'Acapito, F. Xamena and A. Zecchina, *Phys. Chem. Chem. Phys.*, 2003, **5**, 4502–4509.
50 B. Ravel and M. Newville, *J. Synchrotron Radiat.*, 2005, **12**, 537–541.
51 J. J. Kas, A. P. Sorini, M. P. Prange, L. W. Cambell, J. A. Soininen and J. J. Rehr, *Phys. Rev. B: Condens. Matter Mater. Phys.*, 2007, **76**, 195116.
52 S. I. Zabinsky, J. J. Rehr, A. Ankudinov, R. C. Albers and M. J. Eller, *Phys. Rev. B: Condens. Matter Mater. Phys.*, 1995, **52**, 2995–3009.

53 G. Kresse and J. Furthmuller, *Phys. Rev. B: Condens. Matter Mater. Phys.*, 1996, **54**, 11169–11186.
54 G. Kresse and D. Joubert, *Phys. Rev. B: Condens. Matter Mater. Phys.*, 1999, **59**, 1758–1775.
55 J. Hafner, *J. Comput. Chem.*, 2008, **29**, 2044–2078.
56 J. P. Perdew, K. Burke and M. Ernzerhof, *Phys. Rev. Lett.*, 1996, **77**, 3865–3868.
57 G. Smolentsev and A. Soldatov, *J. Synchrotron Radiat.*, 2005, **13**, 19–29.
58 G. Smolentsev and A. V. Soldatov, *Comput. Mater. Sci.*, 2007, **39**, 569–574.
59 J. Kieffer and J. P. Wright, *Powder Diffr.*, 2013, **28**, S339–S350.
60 V. Petříček, M. Dušek and L. Palatinus, *Z. Kristallogr.*, 2014, **229**, 345–352.
61 F. A. Lewis, *Platinum Met. Rev.*, 1982, **26**, 70–78.
62 C. Langhammer, V. P. Zhdanov, I. Zoric and B. Kasemo, *Chem. Phys. Lett.*, 2010, **488**, 62–66.
63 B. Ingham, M. F. Toney, S. C. Hendy, T. Cox, D. D. Fong, J. A. Eastman, P. H. Fuoss, K. J. Stevens, A. Lassesson and S. Brown, *Phys. Rev. B: Condens. Matter Mater. Phys.*, 2008, **78**, 245408.
64 R. Bardhan, L. O. Hedges, C. L. Pint, A. Javey, S. Whitelam and J. J. Urban, *Nat. Mater.*, 2013, **12**, 905–912.
65 T. C. Narayan, A. Baldi, A. L. Koh, R. Sinclair and J. A. Dionne, *Nat. Mater.*, 2016, **15**, 768–776.
66 G. L. Chiarello and D. Ferri, *Phys. Chem. Chem. Phys.*, 2015, **17**, 10579–10591.
67 D. Ferri, M. S. Kumar, R. Wirz, A. Eyssler, O. Korsak, P. Hug, A. Weidenkaff and M. A. Newton, *Phys. Chem. Chem. Phys.*, 2010, **12**, 5634–5646.
68 D. Ferri, M. A. Newton, M. Di Michiel, G. L. Chiarello, S. Yoon, Y. Lu and J. Andrieux, *Angew. Chem., Int. Ed.*, 2014, **53**, 8890–8894.
69 A. I. Frenkel, C. W. Hills and R. G. Nuzzo, *J. Phys. Chem. B*, 2001, **105**, 12689–12703.
70 A. I. Frenkel, A. Yevick, C. Cooper and R. Vasic, *Annu. Rev. Anal. Chem.*, 2011, **4**, 23–39.
71 A. I. Frenkel, *Chem. Soc. Rev.*, 2012, **41**, 8163–8178.
72 G. Agostini, R. Pellegrini, G. Leofanti, L. Bertinetti, S. Bertarione, E. Groppo, A. Zecchina and C. Lamberti, *J. Phys. Chem. C*, 2009, **113**, 10485–10492.
73 G. Agostini, E. Groppo, A. Piovano, R. Pellegrini, G. Leofanti and C. Lamberti, *Langmuir*, 2010, **26**, 11204–11211.
74 G. Agostini, A. Piovano, L. Bertinetti, R. Pellegrini, G. Leofanti, E. Groppo and C. Lamberti, *J. Phys. Chem. C*, 2014, **118**, 4085–4094.
75 M. Manzoli, F. Vindigni, T. Tabakova, C. Lamberti, D. Dimitrov, K. Ivanov and G. Agostini, *J. Mater. Chem. A*, 2017, **5**, 2083–2094.
76 A. L. Bugaev, A. A. Guda, K. A. Lomachenko, A. Lazzarini, V. V. Srabionyan, J. G. Vitillo, A. Piovano, E. Groppo, L. A. Bugaev, A. V. Soldatov, V. P. Dmitriev, R. Pellegrini, J. A. van Bokhoven and C. Lamberti, *J. Phys.: Conf. Ser.*, 2016, **712**, 012032.
77 R. Campesi, F. Cuevas, R. Gadiou, E. Leroy, M. Hirscher, C. Vix-Guterl and M. Latroche, *Carbon*, 2008, **46**, 206–214.
78 T. B. Flanagan and W. A. Oates, *Annu. Rev. Anal. Chem.*, 1991, **21**, 269–304.
79 R. Griessen, N. Strohfeldt and H. Giessen, *Nat. Mater.*, 2016, **15**, 311–317.
80 A. Zuttel, C. Nutzenadel, G. Schmid, C. Emmenegger, P. Sudan and L. Schlapbach, *Appl. Surf. Sci.*, 2000, **162**, 571–575.

81 A. Baldi, T. C. Narayan, A. L. Koh and J. A. Dionne, *Nat. Mater.*, 2014, **13**, 1143–1148.
82 S. Syrenova, C. Wadell, F. A. A. Nugroho, T. A. Gschneidtner, Y. A. D. Fernandez, G. Nalin, D. Switlik, F. Westerlund, T. J. Antosiewicz, V. P. Zhdanov, K. Moth-Poulsen and C. Langhammer, *Nat. Mater.*, 2015, **14**, 1236–1244.
83 C. Zlotea, F. Cuevas, V. Paul-Boncour, E. Leroy, P. Dibandjo, R. Gadiou, C. Vix-Guterl and M. Latroche, *J. Am. Chem. Soc.*, 2010, **132**, 7720–7729.
84 G. B. Kistiakowsky and A. G. Nickle, *Discuss. Faraday Soc.*, 1951, **10**, 175–187.
85 G. B. Kistiakowsky, H. Romeyn, J. R. Ruhoff, H. A. Smith and W. E. Vaughan, *J. Am. Chem. Soc.*, 1935, **57**, 65–75.
86 A. L. Bugaev, O. A. Usoltsev, A. A. Guda, K. A. Lomachenko, I. A. Pankin, Y. V. Rusalev, H. Emerich, E. Groppo, R. Pellegrini, A. V. Soldatov, J. A. van Bokhoven and C. Lamberti, *J. Phys. Chem. C*, 2018, **122**, DOI: 10.1021/acs.jpcc.7b11473.